

Low-energy spectrum of double-junction superconducting circuits in the Born-Oppenheimer approximation

Leo Uhre Jakobsen,^{1,2} Ksenia Shagalov,^{1,2} David Feldstein-Bofill,^{1,2}
Morten Kjaergaard,^{1,2} Karsten Flensberg,¹ and Svend Krøjer^{1,2}

¹*Center for Quantum Devices, Niels Bohr Institute, University of Copenhagen, Denmark*

²*NNF Quantum Computing Programme, Niels Bohr Institute, University of Copenhagen, Denmark*

(Dated: March 30, 2026)

The superconductor–insulator–superconductor Josephson junction is the fundamental nonlinear element of superconducting circuits. Connecting two junctions in series gives rise to higher-harmonic content in the total energy-phase relation, enabling new design opportunities in multimode circuits. However, the double-junction element hosts an internal mode whose spectrum is set by the finite capacitances of the individual junctions. Using a Born–Oppenheimer approximation that treats the additional mode as fast compared to the qubit mode, we analyze the double-junction circuit element shunted by a large capacitor. Here, we derive an effective single-mode model of the qubit containing a correction term owing to the presence of the internal mode. We explore experimentally relevant parameter regimes and find that our model accurately describes the low-energy spectrum of the qubit. We further discuss how eliminating the internal degree of freedom affects the system’s periodic boundary conditions and how this leads to non-uniqueness in performing the Born–Oppenheimer approximation. Finally, we analyze the harmonic content of the double-junction element and discuss its sensitivity to charge noise.

I. INTRODUCTION

Superconducting circuits constitute a versatile and flexible platform for quantum metrology, quantum-limited amplification, and quantum processors [1–6]. The Josephson junction, typically realized as a superconductor-insulator-superconductor (SIS) junction, is the fundamental nonlinear element enabling these technologies [7, 8]. For example, the nonlinearity of a single junction shunted by a large capacitor or a large inductor leads to the weakly anharmonic transmon qubit [9] and strongly anharmonic fluxonium qubit [10], respectively. Beyond these conceptually simple single-mode qubits, superconducting circuits based on multiple Josephson junctions allow for the engineering of multi-mode devices, often introducing original design opportunities. Examples count various noise-protected superconducting qubits [11–24], readout techniques beyond conventional dispersive readout [25–31], flexible mixing and coupling elements [32–35], and general Josephson harmonics engineering [36]. Here, Josephson harmonics engineering represents a particularly flexible way to use multiple junctions to, in principle, realize any energy-phase relation of the resultant two-terminal multi-mode circuit. This idea builds on the experimentally verified [23, 31, 37, 38] insight that two junctions in series give rise to a non-sinusoidal energy-phase relation which can be used as a resource of higher Josephson harmonics.

A common obstacle when working with multi-mode circuits is that they often require approximations to reduce the number of degrees of freedom at the level of the Hamiltonian [16, 19–21, 24, 32]. Such simplifications are important since they increase intuition, guide execution, and interpretation of experiments and significantly reduce computational overhead in simulations. Multi-mode

devices are typically designed and realized such that the low-energy physics is described by a single primary mode, while internal high-energy modes only participate indirectly. In this case, the internal modes can be “integrated out” to yield an effective Hamiltonian where the primary mode(s) is(are) renormalized by the additional modes [39]. In a classical approximation, the internal modes are assumed to be fixed via energy minimization, neglecting their quantum zero-point fluctuations. This approach typically works well for harmonic modes without external capacitors, since the intrinsic capacitance of inductors is vanishingly small, leading to highly localized zero-point fluctuations and a very high excitation energy [19, 20, 24]. However, for periodic modes whose inductive energy is set by Josephson junctions, the intrinsic junction capacitance can be appreciable in experiments, resulting in increased zero-point fluctuations and decreased excitation energy of the internal modes [23, 31]. In this case, the classical approximation is not guaranteed to be accurate, and methods that take into account the quantum dynamics of the auxiliary modes are required.

Beyond classical approaches, the Born–Oppenheimer (BO) approximation has proved useful in the study of multi-mode qubits to systematically account for zero-point fluctuations of high-energy modes [16, 21, 23, 31, 40]. The BO approximation assumes high-energy “fast” modes are in the ground state such that the corresponding energy depends parametrically on the low-energy “slow” modes, effectively renormalizing the potential energy of the slow modes [39, 40]. When the BO approximation is applied to degrees of freedom with periodic boundary conditions, such as high-energy transmon modes, it raises practical questions about how the system’s periodicity should be interpreted as the number of degrees of freedom is reduced.

In this work, we consider a two-terminal double-

junction circuit element and derive an effective single-mode model by integrating out its internal mode as shown schematically in Fig. 1(a,c). We obtain the circuit's effective energy-phase relation renormalized by the internal mode via the BO approximation and perform a detailed numerical analysis of the parameter space of validity by comparing to the full two-mode model. We discuss how the periodic boundary conditions are treated in the BO approximation and find that the two-mode model can be significantly simplified before applying the BO approximation. We also analyze how the Josephson harmonics are renormalized and quantify how the charge noise sensitivity of the auxiliary mode is inherited by the primary qubit mode. With this analysis, the double-junction element can be considered as a single higher-harmonic component that can be readily utilized when developing superconducting circuits.

The paper is organized as follows: In Sec. II, we introduce the double-junction circuit and review the classical single-mode model, including its harmonics. In Sec. III, we give a full two-mode description of the circuit. We review the BO approximation and obtain the analytical BO correction to the classical model. In Sec. IV, we investigate the accuracy of the BO single-mode model, its higher Josephson harmonics, and the charge dispersion due to offset charges on the central superconducting island. In Sec. V, we summarize the results of the paper.

II. BACKGROUND

The double-junction circuit consists of a large shunting capacitance C in parallel with two junctions E_{J1}, E_{J2} in series, see Fig. 1(a). The phase difference across the two junctions constitute the qubit degree of freedom ϕ while the presence of the middle island gives rise to an auxiliary degree of freedom, which we refer to as the internal mode θ . The frequencies of the two modes are determined by their respective charging energies, which are determined by the large shunting capacitor for the qubit mode and by the smaller junction capacitances C_{J1}, C_{J2} for the internal mode. The intrinsic junction capacitances are set by the junction overlap area ($100 \times 100 \text{ nm}^2$ scale) corresponding to junction capacitances approximately one order of magnitude less than the typical shunting capacitances used in transmon qubits [7, 31, 41]. For experimentally relevant parameters, the charging energy of the internal mode will therefore be significantly larger than for the qubit mode. Consequently, double-junction transmons have several excitations of the qubit mode at energies below the first excited state of the internal mode, see Fig. 1(b,e). This means that an effective single-mode model that describes the low-energy excitations of the qubit well can be obtained by assuming the internal mode is in its ground state [39].

When excitations in the internal mode are excluded, tunneling across the two junctions is correlated, and as a consequence, the two junctions in series can be considered

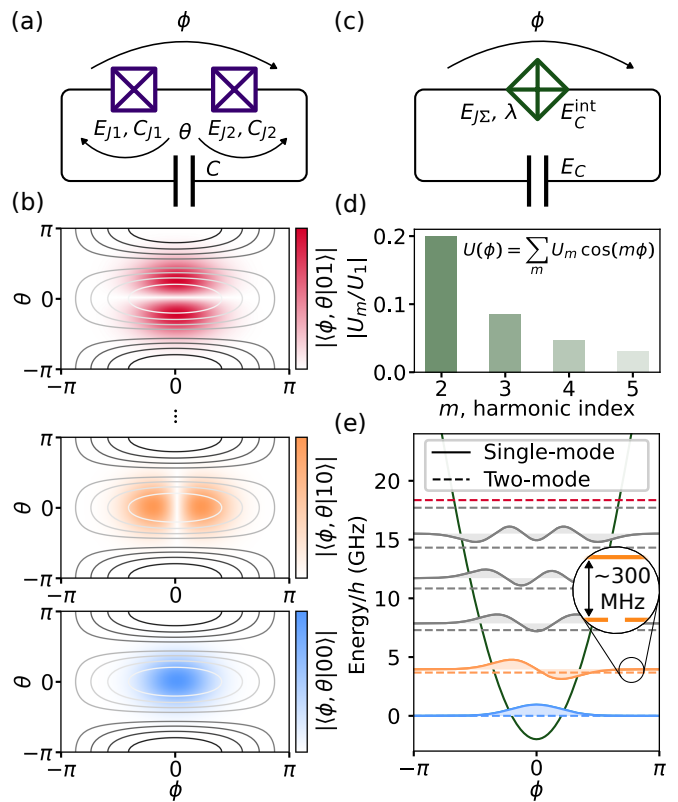


FIG. 1. The double-junction circuit as a single effective element. (a) Circuit diagram of the double-junction qubit with two Josephson junctions in series, shunted by a large capacitor. A low-energy qubit mode, ϕ , and a high-energy internal mode, θ , are shown with relevant circuit parameters. (b) Phase basis wavefunctions of the ground state (blue, bottom), the first qubit excitation (orange, middle) and the first internal mode excitation (red, top). Contour lines indicate the double-junction potential (Eq. (8)). (c) An effective single-element representation of the double-junction circuit describing the qubit mode using the total Josephson energy E_{JS} and junction asymmetry λ . (d) Appreciable higher harmonic coefficients extracted from the classical single-mode model (Eq. (2)). (e) Qubit wavefunctions of the classical single-mode model (solid lines, effective potential energy in dark green) compared to the full two-mode model (dashed lines, first internal mode excitation in red), showing significant discrepancies of the classical model. The parameters are representative of realistic device parameters; $E_{J1}/h = E_{J2}/h = 20 \text{ GHz}$, $E_C^{\text{int}}/h = 1.25 \text{ GHz}$ ($C_{J1} = C_{J2} \approx 8 \text{ fF}$), $E_C/h = 200 \text{ MHz}$ ($C \approx 93 \text{ fF}$).

a single effective element, see Fig. 1(c). The correlated tunneling across this effective element admits higher-order tunneling of Cooper pairs (i.e. pairs of Cooper pairs), corresponding to higher Josephson harmonics in the single-mode energy-phase relation

$$U(\phi) = \sum_m U_m \cos(m\phi), \quad (1)$$

where U_m are the Josephson harmonic coefficients, see Fig. 1(d). The effective energy-phase relation $U(\phi)$ can

be estimated in a classical approximation where the internal mode is assumed to be fixed to the value that minimizes the classical energy [36], giving the result

$$U_{\text{classical}}(\phi) = -E_{J\Sigma} \sqrt{1 - \lambda \sin^2 \frac{\phi}{2}}. \quad (2)$$

Here, $E_{J\Sigma} = E_{J_1} + E_{J_2}$ is the sum of the Josephson energies and $\lambda = 4E_{J_1}E_{J_2}/(E_{J_1} + E_{J_2})^2$ is the junction asymmetry parameter, which is unity for $E_{J_1} = E_{J_2}$. In this *balanced* case, the second harmonic of $U_{\text{classical}}$ can become as large as 20% of the fundamental harmonic, see Fig. 1(d).

As pointed out in Ref. [36], there is a striking analogy between Eq. (2) and the energy-phase relation of a semiconductor-based junction [42]

$$U_{\text{semi}}(\phi) = -\Delta \sum_i \sqrt{1 - T_i \sin^2 \frac{\phi}{2}}, \quad (3)$$

where the junction asymmetry λ plays the role of the transmission probability T_i of Andreev processes and $E_{J\Sigma}$ plays the role of the superconducting gap Δ . Although this analogy is attractive, it is not an exact equivalence due to the dynamics of the internal mode in the double-junction circuit, which is neglected in Eq. (2). By comparing the low-energy spectrum of the single-mode model in Eq. (2) to the full two-mode model (Eq. (4) below), we find a discrepancy in the qubit frequency of around ~ 300 MHz for realistic parameters that put the qubit mode in the transmon regime, see Fig. 1(e). In the next section, we start from the full two-mode model describing the qubit and internal mode and perform a BO approximation in order to obtain a single mode model that accounts for the renormalization due to the internal mode.

III. THEORY

A. Two-mode model

We start with the full two-mode Hamiltonian of the double-junction circuit as obtained from standard circuit quantization [39, 43]. This enables us to take into account the zero-point fluctuations of the internal mode. The two-mode Hamiltonian is

$$H = 4E_{C_1}(n_1 - n_{g_1})^2 + 4E_{C_2}(n_2 - n_{g_2})^2 + gn_1n_2 - E_{J_1} \cos(\varphi_1) - E_{J_2} \cos(\varphi_2). \quad (4)$$

Here, the Hamiltonian is given in terms of the individual phase drops across the two junctions φ_1, φ_2 and their conjugate Cooper pair number operators n_1, n_2 . For each Cooper pair number operator, there is an associated offset charge n_{g_1}, n_{g_2} . The charging energies are given by $E_{C_1} = e^2(C + C_{J_2})/2C_\Sigma^2$, $E_{C_2} = e^2(C + C_{J_1})/2C_\Sigma^2$, and $g = 4e^2C/C_\Sigma^2$ where $C_\Sigma^2 = C(C_{J_1} + C_{J_2}) + C_{J_1}C_{J_2}$.

In order to obtain a single mode description of the qubit degree of freedom, we transform the variables to diagonalize the capacitive term in the Hamiltonian. The transformation is

$$\phi' = \mathbf{S}^T \phi, \quad \mathbf{n}' = \mathbf{S}^{-1} \mathbf{n}, \quad (5)$$

$$\begin{pmatrix} \phi \\ \theta \end{pmatrix} = \begin{pmatrix} 1 & 1 \\ \frac{k+1}{2} & \frac{k-1}{2} \end{pmatrix} \begin{pmatrix} \varphi_1 \\ \varphi_2 \end{pmatrix}, \quad (6)$$

$$\begin{pmatrix} n \\ N \end{pmatrix} = \begin{pmatrix} \frac{1-k}{2} & \frac{1+k}{2} \\ 1 & -1 \end{pmatrix} \begin{pmatrix} n_1 \\ n_2 \end{pmatrix}, \quad (7)$$

where $k = (C_{J_1} - C_{J_2})/(C_{J_1} + C_{J_2})$ is the junction capacitance asymmetry. This non-orthogonal, but canonical, transformation is inspired by Ref. [40] and preserves the qubit mode as the sum of the junction phase differences $\phi = \varphi_1 + \varphi_2$. This is important as we seek a description of the two junctions as a single effective element that can be used with external circuitry. Additionally, the transformation preserves the phase space volume of phase and charge separately since $|\det \mathbf{S}| = 1$.

The Hamiltonian resulting from the transformation in Eq. (5) is

$$H' = 4E_C(n - n_g)^2 + 4E_C^{\text{int}}(N - N_g)^2 - E_{J\Sigma} \cos \frac{\phi}{2} \cos(\theta - k \frac{\phi}{2}) - E_{J\Delta} \sin \frac{\phi}{2} \sin(\theta - k \frac{\phi}{2}), \quad (8)$$

where the charging energies associated with the qubit and internal modes are $E_C = e^2/2(C + C_{J_1}C_{J_2}/(C_{J_1} + C_{J_2}))$ and $E_C^{\text{int}} = e^2/2(C_{J_1} + C_{J_2})$ while $E_{J\Sigma} = E_{J_1} + E_{J_2}$, $E_{J\Delta} = E_{J_1} - E_{J_2}$ are the sum and differences of the Josephson energies. The qubit and internal mode offset charges n_g, N_g are suitable redefinitions of n_{g_1}, n_{g_2} and the potential energy in Eq. (8) is shown in Fig. 2(a). Despite the apparent asymmetry in the definition of ϕ, θ in Eq. (5), the two modes can be faithfully interpreted as representing the dynamics of the qubit island and middle island; the qubit mode experiences the shunting capacitance C in parallel to the junction capacitances C_{J_1}, C_{J_2} in series, while the internal mode experiences the junction capacitances in parallel. Finally, the transformation also couples the boundary conditions of the ϕ - and θ -modes, as we discuss in Sec. III C.

B. Born-Oppenheimer approximation

The goal is now to integrate out the internal θ -mode from the transformed Hamiltonian in Eq. (8) using the BO approximation. This will result in a correction term arising from the internal mode zero-point fluctuations that adds to the classically obtained energy-phase relation $U_{\text{classical}}(\phi)$. As a reminder, the BO approximation separates the fast (internal) and slow (qubit) modes using an ansatz wavefunction and Hamiltonian of the form [16, 39, 40]

$$\Psi_{\text{ansatz}} = \chi^\phi(\theta)\psi(\phi), \quad (9)$$

$$H_{\text{ansatz}} = H_{\text{slow}}(\phi) + H_{\text{fast}}^\phi(\theta). \quad (10)$$

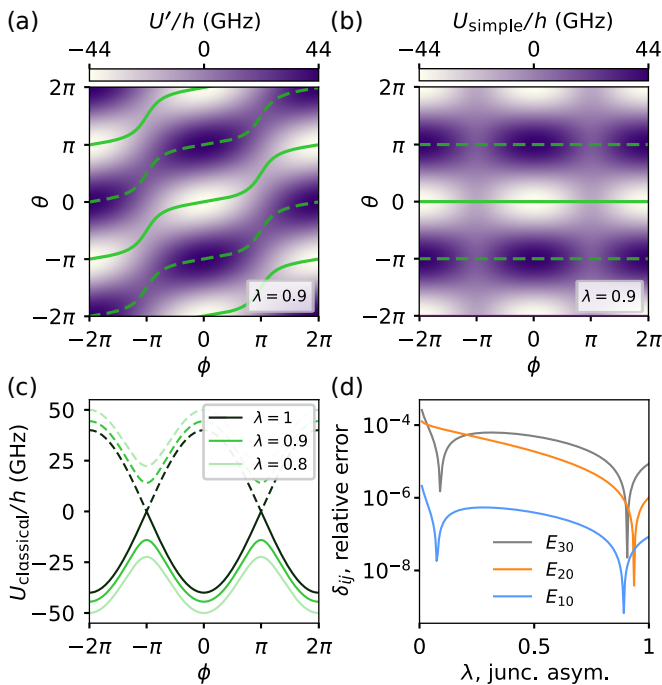


FIG. 2. Potential energy of (a) the double-junction circuit (Eq. (8)) and (b) the simplified potential (Eq. (16)) for junction asymmetry $\lambda = 0.9$. The lines of minimal and maximal potential energy as a function of ϕ are shown in solid and dashed green, respectively. The simplified potential preserves the potential in the θ -direction while the minima line is aligned to $\theta = 0$. (c) The potential energy along the minimal (solid) and maximal (dashed) lines from (a-b) for different values of the junction asymmetry λ . (d) The relative numerical error δ_{ij} of low-energy levels between the original and simplified potentials from (a-b), showing the simplified potential reproduces the same low-energy spectrum as the original potential to high accuracy. We fix $E_C/h = 200$ MHz, $\lambda E_{J\Sigma}/4 = 50E_C$ and $E_{J\Sigma}/E_C^{\text{int}} = 32$ as λ is varied.

The slow mode enters parametrically (indicated by superscript) in the ansatz wavefunction and the Hamiltonian describing the fast mode. A low-energy Hamiltonian that only describes the slow mode is then obtained by assuming that the fast mode is in its ground state

$$H_{\text{ansatz}} \Psi_{\text{ansatz}} = [H_{\text{slow}}(\phi) + H_{\text{fast}}^{\phi}(\theta)] \chi^{\phi}(\theta) \psi(\phi) \quad (11)$$

$$\rightarrow H_{\text{BO}} \psi(\phi) = [H_{\text{slow}}(\phi) + U_{\text{corr}}(\phi)] \psi(\phi), \quad (12)$$

where the BO correction potential U_{corr} is the ground state energy of H_{fast} with ϕ promoted to a quantum variable again.

In the next section, we discuss the implications for the coupled, periodic boundary conditions as the BO approximation separates the slow and fast modes.

C. Simplifying boundary conditions

The original boundary conditions are 2π -periodic in φ_1 and φ_2 which translates to a coupled boundary condition for the qubit and internal mode

$$(\phi, \theta) = (\phi + 2\pi, \theta \pm \pi + \pi k), \quad (13)$$

for $\varphi_1 \rightarrow \varphi_1 + 2\pi$ (positive sign) or $\varphi_2 \rightarrow \varphi_2 + 2\pi$ (negative sign). As the BO approximation separates the slow and fast modes, their coupled boundary conditions also decouple, and the resulting potential $U_{\text{BO}}(\phi) = U_{\text{classical}}(\phi) + U_{\text{corr}}(\phi)$ preserves the original 2π -periodicity of the ϕ -mode independent of the boundary condition of the θ -mode. This implies that the single-mode BO potential U_{BO} can arise from a family of two-mode ansatz potentials with different coupled boundary conditions. To see this explicitly, we rewrite the potential in Eq. (8) using standard trigonometric identities

$$U'(\phi, \theta) = -s(\phi) E_{J\Sigma} \cos(\theta - f(\phi)) \sqrt{1 - \lambda \sin^2 \frac{\phi}{2}}, \quad (14)$$

$$f(\phi) = k \frac{\phi}{2} + \arctan \left(\frac{E_{J\Delta}}{E_{J\Sigma}} \tan \frac{\phi}{2} \right), \quad (15)$$

where $s(\phi) = \text{sign}[\cos(\phi/2)]$ is a sign, see also Fig. 2(a) for a plot of U' . As ϕ is reduced to a parameter and the fast mode is assumed to be in its ground state, both the parameters f^{ϕ} and s^{ϕ} are absorbed by the fast mode, which always localizes at its minimum $\theta_{\text{min}}^{\phi} = f^{\phi} + \pi(1 - s^{\phi})/2$ (solid green lines in Fig. 2(a,b), dashed green lines correspond to maximum). This means that any (non-diverging) function $f(\phi)$ will reduce to the same single-mode BO potential $U_{\text{BO}}(\phi)$ despite representing different two-mode potentials. We can use this fact to choose a simpler potential U_{simple} in place of U' and use it to compute the BO correction. In the following, we choose $f(\phi) = 0$ and $s = +1$ for the simplified potential

$$U_{\text{simple}}(\phi) = -E_{J\Sigma} \cos \theta \sqrt{1 - \lambda \sin^2 \frac{\phi}{2}}. \quad (16)$$

We make this choice because it explicitly decouples the (ϕ, θ) -boundary condition in Eq. (13), making ϕ and θ 2π -periodic independently. This can be exemplified for $\lambda = 0.9$ ($E_{J2}/E_{J1} \approx 1.9$) by comparing panels (a) and (b) of Fig. 2. In panel (b), we plot U_{simple} where the line along the minima (solid green) is independent of ϕ . We can therefore interpret the simplified potential in Eq. (16) as shifting the minima of the fast mode to zero (mod 2π) for all ϕ and thus decoupling the (ϕ, θ) -boundary condition. Furthermore, the simplified potential also directly admits the solution to the classical potential in Eq. (2) by freezing θ to its minimum value corresponding to $\cos(\theta) = 1$.

In Fig. 2(c), we plot the potential energy along the minima (solid green) and maxima (dashed green) lines

for different junction asymmetries λ . The potential along the minima line is the classically obtained energy-phase relation $U_{\text{classical}}(\phi)$ while the line along the maxima is the unstable classical equilibrium of the θ -mode. Here, we again observe the striking analogy to semiconductor-based junctions; the line along the minima corresponds to U_{semi} and the (unphysical) line of maximal potential energy corresponds to the particle-hole symmetric branch $-U_{\text{semi}}$.

We now investigate the difference between the original potential U' and the simplified potential U_{simple} . Specifically, we are concerned with the effect of varying λ in a configuration of charging and Josephson energies, that places the qubit and internal mode frequencies in the BO regime. We start in the balanced case $\lambda = 1$ and fix a set of parameters that simultaneously put the qubit in a practical regime while satisfying the BO conditions; we set the charging energy of the qubit $E_C/h = 200$ MHz and demand that the qubit is effectively in a transmon regime of $E_J/E_C = 50$. The effective Josephson energy of the qubit mode can be computed from Eq. (14) or Eq. (16) which, together with the transmon requirement, yields the condition $\lambda E_{J\Sigma}/4 = 50E_C$ that specifies $E_{J\Sigma}$ for a given λ . This condition also implicitly determines the qubit frequency which scales as $E_{01}^{\text{qubit}} \sim 1/\sqrt{\lambda}$. We then determine E_C^{int} by choosing a transmon-like regime for the internal mode $E_{J\Sigma}/E_C^{\text{int}} = 32$. Thus, for any λ , the internal mode frequency scales as $E_{01}^{\text{int}} \sim 1/\lambda$, meaning that $E_{01}^{\text{qubit}} < E_{01}^{\text{int}}$ for all $\lambda \leq 1$ as required for the validity of the BO approximation.

In Fig. 2(d), we compare the low-energy spectrum produced by the double-junction potential U' and the simplified potential U_{simple} to verify that the simplified potential faithfully reproduces the low-energy spectrum. For states i , we plot their relative error $\delta_i^{\text{simple}} = |E_i^{\text{simple}} - E_i|/E_i$ of the energies E_i obtained from the exact double-junction potential in Eq. (4) and the energies E_i^{simple} obtained from the approximate and simplified potential in Eq. (16). We observe that the relative error remains below $\lesssim 10^{-4}$, meaning that the simplified potential accurately produces the double-junction spectrum despite the potential being qualitatively different. The sharp minima of very low relative error occur when E_{ij}^{simple} and E_{ij} coincidentally cross, and this behavior therefore depends non-trivially on the physical parameters.

D. Effective single-mode model

We are now in a position to perform the BO approximation of the double-junction circuit. We separate the simplified potential in Eq. (16) into slow and fast poten-

tials to uncover the slow and fast Hamiltonians

$$H_{\text{slow}} = 4E_C(n - n_g)^2 - E_{J\Sigma}\sqrt{1 - \lambda \sin^2 \frac{\phi}{2}}, \quad (17)$$

$$H_{\text{fast}}^\phi = 4E_C^{\text{int}}(N - N_g)^2 + E_{J,\text{eff}}^\phi (1 - \cos \theta), \quad (18)$$

where

$$E_{J,\text{eff}}^\phi = E_{J\Sigma}\sqrt{1 - \lambda \sin^2 \frac{\phi}{2}}, \quad (19)$$

is the effective Josephson energy of the internal mode which depends parametrically on ϕ and gives $E_{J,\text{eff}}^{\phi=0} = E_{J\Sigma}$ consistent with the internal mode experiencing the junctions in parallel. Similarly, an effective Josephson energy of the qubit mode can be found from the curvature of the slow Hamiltonian, $E_{J,\text{eff}}^{\text{slow}} = \lambda E_{J\Sigma}/4 = E_{J1}E_{J2}/(E_{J1} + E_{J2})$, consistent with the qubit mode experiencing the junctions in series.

In the regime $E_{J\Sigma} \gg E_C^{\text{int}}$, the internal mode is localized near the origin and we may approximate $1 - \cos \theta \approx \theta^2/2$ and neglect the internal offset charge N_g . In the harmonic approximation, we obtain the ground state energy of the internal mode, giving the BO correction potential

$$U_{\text{corr}}(\phi) = E_{J\Sigma}\sqrt{\frac{2E_C^{\text{int}}}{E_{J\Sigma}}}\sqrt{1 - \lambda \sin^2 \frac{\phi}{2}}, \quad (20)$$

and the total BO Hamiltonian thus becomes

$$H_{\text{BO}} = 4E_C(n - n_g)^2 + U_{\text{BO}}(\phi), \quad (21)$$

where

$$U_{\text{BO}}(\phi) = U_{\text{classical}}(\phi) + U_{\text{corr}}(\phi). \quad (22)$$

This effective single-mode Hamiltonian is a central result of our work and includes renormalization due to the internal mode through U_{corr} and junction capacitance asymmetry through E_C and E_C^{int} , thus generalizing the results of Refs. [36, 40]. Although this result is obtained in the regime $E_{J\Sigma} \gg E_C^{\text{int}}$, we note that the ground state energy of the fast Hamiltonian in Eq. (18) could also be solved numerically or using Mathieu functions, as is known from the transmon [9]. However, in the non-harmonic regime $E_{J\Sigma}/E_C^{\text{int}} < 30$, the internal mode disperses with the offset charge on the middle island N_g . As we further elaborate in Sec. IV C, this charge dispersion then propagates to the correction potential U_{corr} , resulting in the qubit dispersing significantly with N_g . To avoid this internal mode-mediated dephasing channel, we focus on the parameter regime $E_{J\Sigma}/E_C^{\text{int}} \gtrsim 30$, which also justifies neglecting the offset charge N_g in U_{corr} . In Appendix A, we find that there is no difference in the accuracy of the BO approximation obtained from the harmonic approximation compared to a numerical solution when $E_{J\Sigma}/E_C^{\text{int}} \gtrsim 30$.

In the next section, we analyze the numerical accuracy of the effective single-mode model, its harmonic content, and its sensitivity to offset charge.

IV. RESULTS

A. Accuracy of the Born-Oppenheimer approximation

We now turn to a detailed analysis of the numerical accuracy of the BO single-mode model and compare its performance to the classical single-mode model. We evaluate the numerical accuracy of the single-mode models by using the full two-mode model in Eq. (4) as a reference. For this purpose, we define the cumulative relative error $\Delta_j = \sum_{i=1}^j \delta_i$ of the lowest j qubit levels. Here, $\delta_i = |E'_i - E_i|/E_i$ is the relative error of the energy of the i 'th qubit level as computed using the two-mode model E_i and a single-mode model E'_i . In the following, we explore how well the single-mode models estimate the low-energy qubit spectrum for varying circuit parameters using the cumulative error Δ_j .

In Fig. 3(a), we first plot the cumulative error for the classical and BO models as we increase the number of states that are being taken into account by Δ_j . For the BO model (solid green line), the lowest 5 states are well described as the cumulative relative error is on the 10^{-3} level for the parameters used here (indicated with stars in all panels of the figure and specified in the figure text). Compared to the classical model (dashed line), the BO model performs about two orders of magnitude better in estimating the low-energy qubit spectrum. However, for the higher energy levels (6th and 7th) the cumulative error significantly increases for the BO model. This is because the BO approximation breaks down for levels above the first excited level of the internal mode (red region), which here lies between the 5th and 6th qubit levels. In Appendix A, we resolve the individual relative error for each level and find that they are very similar.

In Fig. 3(b-d), we plot the cumulative error for the lowest three qubit states for varying junction asymmetry λ , internal charging energy E_C^{int} , and capacitance asymmetry k using the same fixed parameters as in Fig. 2. Across all panels, the numerical accuracy of the BO model is on the order of 10^{-3} to 10^{-2} which is about one to two orders of magnitude more accurate than the classical model. In panel (b), we find that the BO model is exceptionally accurate at $\lambda = 1$, corresponding to symmetric junctions. We interpret this as the qubit and internal mode only coupling to second order through the potential at this point, see Eq. (8). In panel (c), we vary the charging energy of the internal mode, which displays an interesting minimum point of the cumulative error for the BO model. For small $E_{J\Sigma}/E_C^{\text{int}}$, the harmonic approximation for the internal mode breaks down, leading to increased error. On the other hand, a large $E_{J\Sigma}/E_C^{\text{int}}$ ratio for fixed $E_{J\Sigma}$, decreases the frequency of the internal mode, making its non-perturbative contribution more relevant despite the BO correction being less important, see Eq. (20). Finally, in panel (d), we vary the capacitance asymmetry for fixed qubit and internal charging energies. Here, the BO model captures this effect well for small $k < 0.2$, but for larger k ,

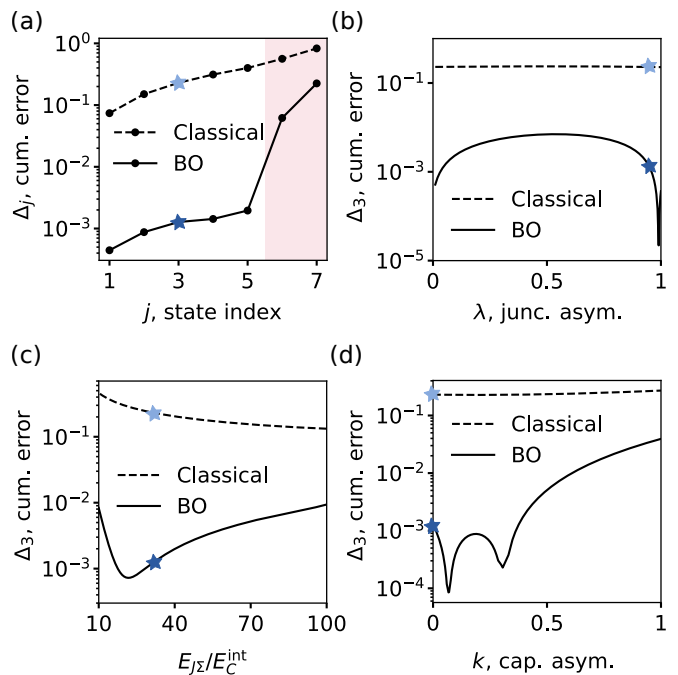


FIG. 3. Comparison of the numerical accuracy of the classical (Eq. (2)) and the BO (Eq. (22)) model. (a) Cumulative error Δ_j relative to the full two-mode model (Eq. (4)) of the lowest j qubit levels, as defined in the main text (Sec. IV A). The first excitation in the internal mode lies between the 5th and 6th qubit levels and the breakdown of the BO model is observed for the states above it (red region). (b-d) Cumulative error of the 3 lowest qubit levels ($j = 3$) as a function of (b) the junction asymmetry λ , (c) the $E_{J\Sigma}/E_C^{\text{int}}$ ratio, and (d) the capacitance asymmetry k . The cumulative error of the BO model remains below $> 10^{-2}$ for most parameter choices and is roughly one to two orders of magnitudes less than the error of the classical model. Stars indicate points of identical configurations across all panels; $j = 3$, $\lambda = 0.95$, $E_{J\Sigma}/E_C^{\text{int}} = 32$, and $k = 0$. Furthermore, $E_C/h = 200$ MHz and $\lambda E_{J\Sigma}/4 = 50E_C$ are fixed for all configurations.

the cumulative error increases. We attribute this to the non-orthogonal transformation in Eq. (5) which becomes significantly skewed for larger k . This can potentially be addressed at the cost of less intuitive analytical results by using an orthogonal transformation to diagonalize the charging terms or via a Bogoliubov transformation.

B. Higher Josephson harmonics

With the effective single-mode model developed in the previous section, we can examine the harmonic content of the potential in the double-junction circuit. The Josephson harmonic coefficients U_m entering Eq. (1) of a potential $U(\phi)$ can be found through

$$U_m = \frac{1}{\pi} \int_{-\pi}^{\pi} U(\phi) \cos(m\phi) d\phi. \quad (23)$$

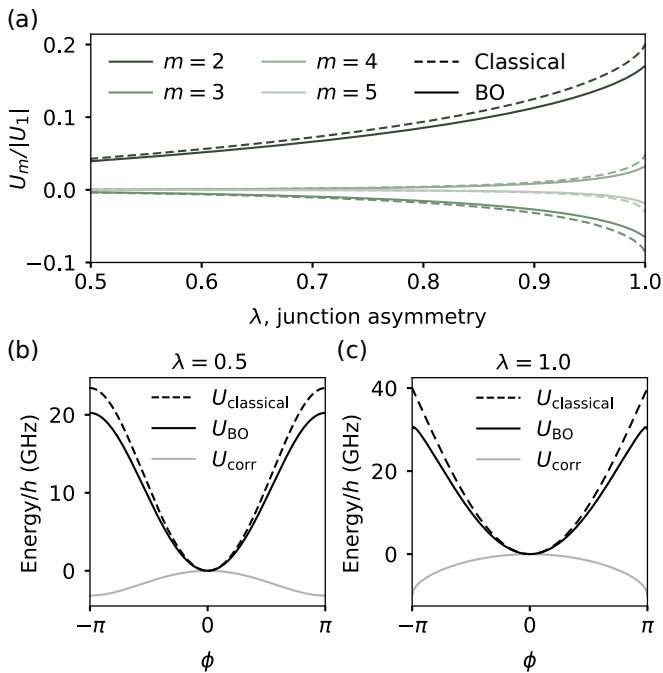


FIG. 4. Harmonics of the single-mode classical and BO potentials. (a) The Josephson harmonic coefficients of the single-mode potential energy in the classical (dashed lines) and BO (solid lines) approximations, showing slightly reduced harmonics for the BO model. Coefficients are scaled to the fundamental frequency coefficient. (b,c) Comparison between the classical (black, dashed), BO (black, solid) and correction (grey, solid) potentials for (b) $\lambda = 0.5$ and (c) $\lambda = 1$. The correction potential becomes increasingly significant for higher energies, consistent with giving a larger correction to higher energy levels. Parameters are $E_C/h = 200$ MHz, $\lambda E_{J\Sigma}/4 = 50E_C$, $E_{J\Sigma}/E_C^{\text{int}} = 32$, and $k = 0$ so $E_C^{\text{int}}/h = 1.25$ GHz for $\lambda = 1$ and $E_C^{\text{int}}/h = 2.5$ GHz for $\lambda = 0.5$.

In Fig. 4(a), we show the higher harmonic coefficients $U_m/|U_1|$ of the classical model Eq. (2) (dashed lines) and the BO potential Eq. (22) (solid lines) as a function of the asymmetry parameter λ . The presence of the fast internal mode, treated by the BO approximation, results in an overall reduction of the higher harmonic content. The second harmonic coefficient $U_2/|U_1|$ reaches a maximum of 0.17 compared to the maximum classical value of 0.2 at $\lambda = 1$.

In Fig. 4(b-c), we further visualize the correction energy $U_{\text{corr}} = U_{\text{BO}} - U_{\text{classical}}$ along with the potential energy seen by the qubit mode ϕ within the two models for (b) $\lambda = 0.5$ and (c) $\lambda = 1$. The potential barrier energy increases significantly with λ in both models, but U_{corr} acts to lower the barrier height in the BO model and alters the ϕ -dependence and, consequently, the harmonic content as seen in panel (a).

In this section, we include the offset charge on the middle island N_g in the BO analysis to evaluate its impact on the qubit mode. In particular, we study the charge dispersion of the qubit to ensure that it is not limited by

the potential dephasing induced by fluctuations in N_g .

The impact of N_g on the fast internal mode is described by a transmon Hamiltonian, see Eq. (18). As is known from the transmon, the eigenenergies E_m disperse with the offset charge according to

$$E_m \approx E_m(N_g = 0) + \varepsilon_m \sin^2(\pi N_g), \quad (24)$$

where ε_m is the peak-to-peak value of the charge dispersion [9], see Fig. 5(a) for the simulated charge dispersion of low-energy states at N_g for $E_{J\Sigma}/E_C^{\text{int}} = 8$. Here, the ground state energy of the internal mode (brown) is computed from Eq. (18) at $\phi = 0$ and displays harmonic dispersion as described by Eq. (24). We also observe the ground (blue) and excited (orange) qubit energies obtained from the full two-mode model in Eq. (4) to disperse in a similar fashion despite not being directly coupled to the charge on the central island N_g .

C. Sensitivity to offset charge

To understand the qubit's dispersion with N_g , we note that, in the context of the BO approximation, the ground state energy E_0 corresponds to the correction potential U_{corr} . The BO correction potential therefore acquires an offset charge dependence

$$U_{\text{corr}}(N_g) \approx U_{\text{corr}}(N_g = 0) + U_{\text{disp}} \sin^2(\pi N_g), \quad (25)$$

where $U_{\text{corr}}(N_g = 0)$ is given by Eq. (20) and U_{disp} is the contribution due to the peak-to-peak value of the charge dispersion ε_0 . This ‘‘dispersion’’ potential contains two parts

$$U_{\text{disp}}(\phi) = \varepsilon_0^{\text{int}} u_{\text{disp}}(\phi), \quad (26)$$

where the ϕ -dependency is collected in

$$u_{\text{disp}}(\phi) = g(\phi)^{\frac{3}{4}} \exp \left[-\sqrt{\frac{8E_{J\Sigma}}{E_C^{\text{int}}}} \left(\sqrt{g(\phi)} - 1 \right) \right], \quad (27)$$

with $g(\phi) = \sqrt{1 - \lambda \sin^2(\phi/2)}$ and where

$$\varepsilon_0^{\text{int}} \approx 2^5 \sqrt{\frac{2}{\pi}} E_C^{\text{int}} \left(\frac{E_{J\Sigma}}{2E_C^{\text{int}}} \right)^{3/4} e^{-\sqrt{8E_{J\Sigma}/E_C^{\text{int}}}}, \quad (28)$$

is an exponentially suppressed prefactor corresponding to the ground state charge dispersion of a transmon with charging energy E_C^{int} and Josephson energy $E_{J\Sigma}$ [9].

In Fig. 5(b), we plot the dispersion potential in Eq. (24) for different values of $E_{J\Sigma}/E_C^{\text{int}}$. We directly observe how the exponentially small prefactor $\varepsilon_0^{\text{int}}$ suppresses the dispersion potential for increasing $E_{J\Sigma}/E_C^{\text{int}}$. This is especially pronounced around $\phi = 0$ which is the relevant region for low-energy qubit states.

To quantitatively assess the impact of the dispersion potential on the qubit energy, we treat U_{disp} as a perturbation to the BO Hamiltonian Eq. (21). First-order perturbation theory then leads to a correction to the qubit

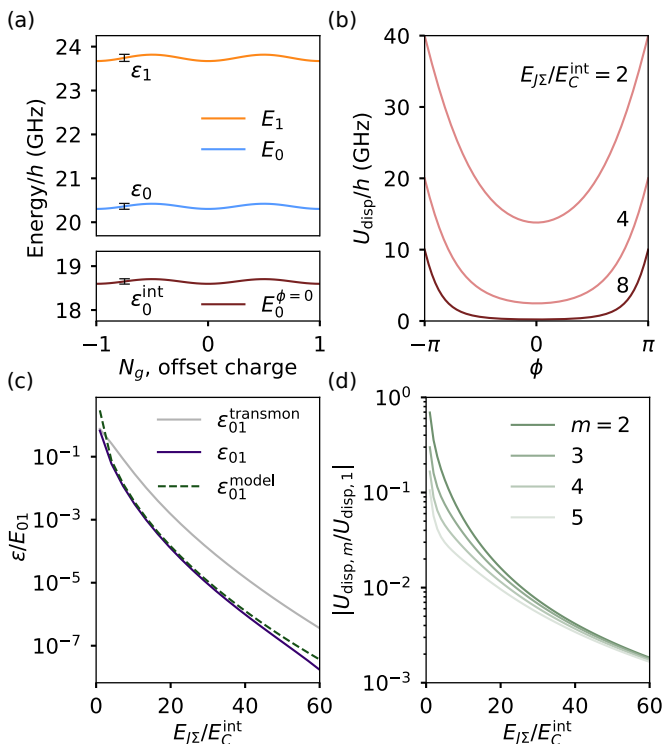


FIG. 5. Numerically obtained charge dispersion of the qubit mediated by the internal mode. (a) Top: Charge dispersion of the internal mode ground state (brown) of the fast Hamiltonian (Eq. (18) at $\phi = 0$) showing peak-to-peak value $\varepsilon_0^{\text{int}}$. Bottom: Charge dispersion of the qubit ground (blue) and first excited (orange) energies of the full two-mode model (Eq. (4)) showing inherited dependence on the offset charge N_g from the internal mode. Parameters used are $E_{J\Sigma}/E_C^{\text{int}} = 8$ to illustrate pronounced N_g -dependence. (b) The dispersive potential (Eq. (26)) shown for different $E_{J\Sigma}/E_C^{\text{int}}$ ratios, displaying exponential suppression for increasing ratios. (c) Peak-to-peak charge dispersion versus $E_{J\Sigma}/E_C^{\text{int}}$ of the qubit (purple, solid) computed from the full two-mode model (Eq. (4)) compared to our first-order model (green, dashed) using the dispersive potential (Eq. (29)). To evaluate $\varepsilon_{01}^{\text{model}}$ we use eigenstates of the BO Hamiltonian (Eq. (21)). We also compare to the charge dispersion of a transmon (grey), observing orders-of-magnitude less charge dispersion of the qubit mode. (d) Fourier coefficients of the dispersion potential U_{disp} , showing suppression below 10^{-2} for $E_{J\Sigma}/E_C^{\text{int}} \gtrsim 30$. For all panels, $\lambda = 1$, $E_C/h = 200$ MHz, $E_{J\Sigma}/h = 40$ GHz.

energies and consequently an expression for the charge dispersion of the qubit mode due to N_g

$$\varepsilon_{01}^{\text{model}} = \varepsilon_0^{\text{int}} [\langle 1 | u_{\text{disp}}(\phi) | 1 \rangle - \langle 0 | u_{\text{disp}}(\phi) | 0 \rangle], \quad (29)$$

which is scaled by the exponentially suppressed $\varepsilon_0^{\text{int}}$, inherited from the internal mode.

In Fig. 5(c), we compare the peak-to-peak charge dispersion of the qubit energy obtained from the full two-mode model in Eq. (4) (purple, solid) to a numerical solution of Eq. (29) (green, dashed) using wavefunctions obtained from the BO Hamiltonian Eq. (21). We find ex-

cellent agreement between the full solution and our first-order perturbative model, showing that the BO approximation can also be used to account for dephasing effects mediated by the internal mode. We also compare these results to the charge dispersion of a standard transmon (gray). We find that the sensitivity to the internal offset charge N_g is suppressed to low-levels comparable to the low sensitivity of transmons for $E_{J\Sigma}/E_C^{\text{int}} \gtrsim 30$. Given the qualitative similarities between the effective model of the double-junction circuit in Eq. (21) and the transmon, we believe that their coherence properties will otherwise be largely the same; however, a complete coherence analysis is beyond the scope of this work.

In Fig. 5(d), we finally plot the lowest harmonics of the dispersion potential U_{disp} as a function of $E_{J\Sigma}/E_C^{\text{int}}$. We find that they are sufficiently suppressed ($< 10^{-2}$) for $E_{J\Sigma}/E_C^{\text{int}} \gtrsim 30$, meaning that the higher lying states and harmonics analysis is not impacted by the dispersion potential. In conclusion, our analysis shows that the offset charge on the middle island N_g can be neglected for $E_{J\Sigma}/E_C^{\text{int}} \gtrsim 30$.

V. CONCLUSIONS

We present an effective single-mode model to accurately describe the low-energy qubit spectrum of a double-junction element shunted by a large capacitor. Using the BO approximation, we obtain a correction term to the effective potential energy coming from zero-point fluctuations of the double-junction element's internal degree of freedom. We analyze the numerical accuracy of the BO model for experimentally relevant parameter regimes and find that the inclusion of the correction term decreases the error in the numerically obtained low-energy qubit spectrum by two orders of magnitude. Supporting these results are two parallel experimental works on double-junction qubits [23, 31]. In these works, the BO single-mode model obtained here is required to accurately fit the respective qubit spectra. In Ref. [31] the relative junction energy of an all-SIS double-junction transmon is tuned in-situ via flux control to experimentally probe in which parameter regimes the effective single-mode model describes the observed data. In Ref. [23] the double-junction element is placed in parallel to a semiconductor-based junction such that interference between the two arms leads to controllable higher Josephson harmonics, illustrating how the double-junction element can be used as an effective single component.

This work further extends the analysis to the offset charge dispersion of the internal degree of freedom. We find a transmon regime ($E_{J\Sigma}/E_C^{\text{int}} \gtrsim 30$) for the internal mode, which exponentially suppresses the sensitivity of the qubit mode to internal offset charges. These results enable us to analyze the harmonic content of the double-junction element, and we find that the correction term only slightly decreases the overall content of higher Josephson harmonics. Finally, our analysis reveals

that a family of potential energies gives rise to the same BO correction term. This enables a simplified approach when performing the BO approximation; first, simplify the multi-mode potential within the family of interest, and second, perform the conventional steps in the BO approximation. In summary, our analysis and results show that the double-junction element can be readily used as a resource for higher Josephson harmonics in multi-mode circuits and further validate the BO approximation as a powerful tool for studying multi-mode superconducting circuits.

ACKNOWLEDGMENTS

We gratefully acknowledge useful discussions with Clinton A. Potts, Valla Fatemi, András Gyenis, Natalia Zhurbina, Christian Kraglund Andersen, Adrián Parra-Rodríguez, Benjamin Leviatan, Alexandre Blais, Cheng-Li Chen, and Kohei Matsuura.

This research was supported by the Novo Nordisk Foundation (grant no. NNF22SA0081175), the NNF Quantum Computing Programme (NQCP), Villum Foundation through a Villum Young Investigator grant (grant no. 37467), the Innovation Fund Denmark (grant no. 2081-00013B, DanQ), the U.S. Army Research Office (grant no. W911NF-22-1-0042, NHyDTech), by the European Union through an ERC Starting Grant, (grant no. 101077479, NovADePro), and by the Carlsberg Foundation (grant no. CF21-0343). Any opinions, findings, conclusions or recommendations expressed in this material are those of the author(s) and do not necessarily reflect the views of Army Research Office or the US Government. Views and opinions expressed are those of the author(s) only and do not necessarily reflect those of the European Union or the European Research Council. Neither the European Union nor the granting authority can be held responsible for them. Finally, we gratefully acknowledge Lena Jacobsen and Helle Grunnet for program management support.

Appendix A: Numerical Born-Oppenheimer approximation

In this appendix, we analyze the numerical solution of the fast Hamiltonian Eq. (18) and compare it to the analytically obtained solution in Eq. (20). The numerical solutions refer to solving for the ground state energy of the fast mode in Eq. (18) for an array of values ϕ . This ground state energy then constitutes the correction potential in Eqs. (20) and (21). Using this numerically obtained correction potential, the single-mode qubit states and energies are then computed numerically as for the analytically obtained correction potential.

In Fig. A1, we compare the accuracy of the numerical BO model with the results of Fig. 3. Across all panels, we observe that the accuracy of the numerical and ana-

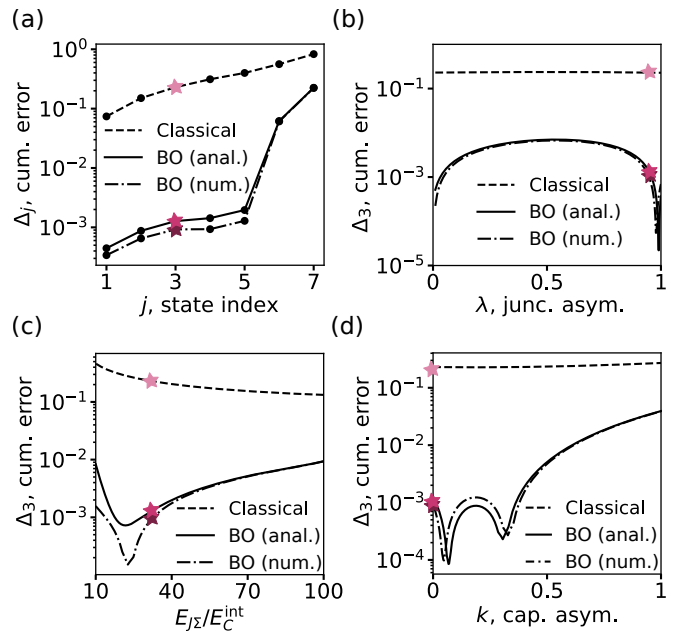


FIG. A1. Comparison of the accuracy of the single-mode BO Hamiltonian (Eq. (21)) when the fast Hamiltonian (Eq. (18)) is solved analytically (Eq. (20)) or numerically. Parameters used are identical to Fig. 3.

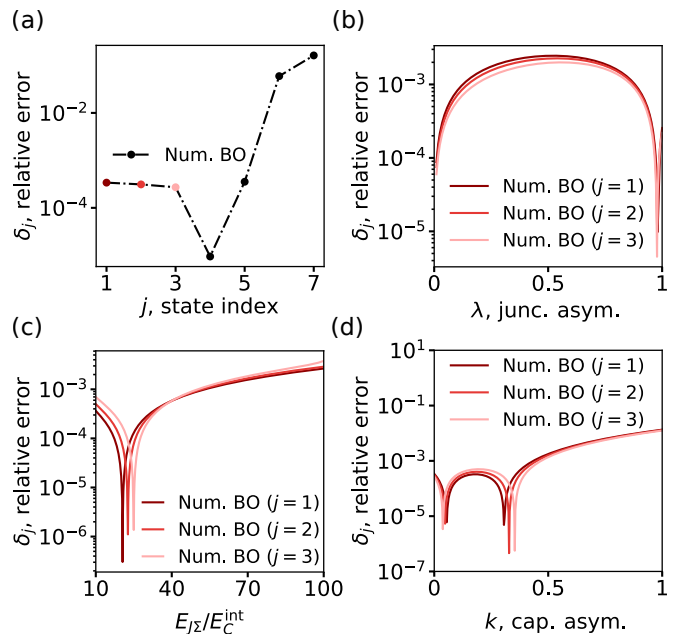


FIG. A2. The individual relative errors of the lowest levels in the numerical BO model. Parameters used are identical to Figs. 3 and A1.

lytical BO models is very similar. Only in panel (c) for values of $E_{J\Sigma}/E_C^{\text{int}}$ below 30, does the numerical model slightly outperform the analytical model. This is a consequence of the harmonic approximation used in the analytical model failing for lower values of $E_{J\Sigma}/E_C^{\text{int}}$. The numerical solution performs better as it directly solves for

the ground state energy without making any additional assumptions. However, as argued in Sec. IV C, the practical parameter regime of interest lies at $E_{J\Sigma}/E_C^{\text{int}} \gtrsim 30$ and for this reason we focus on the simpler analytical BO model in this work.

In Fig. A2, we resolve the cumulative errors of the numerical solution in Fig. A1 and plot the individual relative error δ_j as defined in Sec. IV A. Across all panels, we observe very similar relative errors for the lowest three ex-

citation energies. Only the position of the very low relative error dips is state dependent. These dips correspond to parameter values where the energies from the single-mode BO model and the full two-mode model coincide. The position of these dips therefore depends non-trivially on the state index and parameters used. The very low relative error of $j = 4$ in panel (a) is another example of this. In the cumulative errors shown in Fig. A1, the combinations of these dips give rise to slight kinks in panels (c) and (d).

-
- [1] M. Kjaergaard, M. E. Schwartz, J. Braumüller, P. Krantz, J. I.-J. Wang, S. Gustavsson, and W. D. Oliver, *Annual Review of Condensed Matter Physics* **11**, 369 (2020).
- [2] P. Krantz, M. Kjaergaard, F. Yan, T. P. Orlando, S. Gustavsson, and W. D. Oliver, *Applied Physics Reviews* **6**, 021318 (2019).
- [3] A. A. Clerk, M. H. Devoret, S. M. Girvin, F. Marquardt, and R. J. Schoelkopf, *Rev. Mod. Phys.* **82**, 1155 (2010).
- [4] A. Blais, A. L. Grimsmo, S. M. Girvin, and A. Wallraff, *Reviews of Modern Physics* **93**, 025005 (2021).
- [5] C. L. Degen, F. Reinhard, and P. Cappellaro, *Rev. Mod. Phys.* **89**, 035002 (2017).
- [6] M. Esposito, A. Ranadive, L. Planat, and N. Roch, *Applied Physics Letters* **119**, 120501 (2021).
- [7] H. Kim, G. Jang, S. Jin, D. Shin, H.-J. Shin, J. Luo, I. Siddiqi, Y. Kim, H. H. Yoon, and L. B. Nguyen, *arXiv preprint arXiv:2505.12724* (2025).
- [8] I. Siddiqi, *Nature Reviews Materials* **6**, 875 (2021).
- [9] J. Koch, T. M. Yu, J. Gambetta, A. A. Houck, D. I. Schuster, J. Majer, A. Blais, M. H. Devoret, S. M. Girvin, and R. J. Schoelkopf, *Physical Review A—Atomic, Molecular, and Optical Physics* **76**, 042319 (2007).
- [10] V. E. Manucharyan, J. Koch, L. I. Glazman, and M. H. Devoret, *Science* **326**, 113 (2009).
- [11] A. Gyenis, A. Di Paolo, J. Koch, A. Blais, A. A. Houck, and D. I. Schuster, *PRX quantum* **2**, 030101 (2021).
- [12] B. Douçot and L. B. Ioffe, *Reports on Progress in Physics* **75**, 072001 (2012).
- [13] M. T. Bell, J. Paramanandam, L. B. Ioffe, and M. E. Gershenson, *Phys. Rev. Lett.* **112**, 167001 (2014).
- [14] P. Brooks, A. Kitaev, and J. Preskill, *Phys. Rev. A* **87**, 052306 (2013).
- [15] P. Groszkowski, A. D. Paolo, A. L. Grimsmo, A. Blais, D. I. Schuster, A. A. Houck, and J. Koch, *New Journal of Physics* **20**, 043053 (2018).
- [16] A. D. Paolo, A. L. Grimsmo, P. Groszkowski, J. Koch, and A. Blais, *New Journal of Physics* **21**, 043002 (2019).
- [17] A. Gyenis, P. S. Mundada, A. Di Paolo, T. M. Hazard, X. You, D. I. Schuster, J. Koch, A. Blais, and A. A. Houck, *PRX Quantum* **2**, 010339 (2021).
- [18] K. Kalashnikov, W. T. Hsieh, W. Zhang, W.-S. Lu, P. Kamenov, A. Di Paolo, A. Blais, M. E. Gershenson, and M. Bell, *PRX Quantum* **1**, 010307 (2020).
- [19] W. Smith, A. Kou, X. Xiao, U. Vool, and M. Devoret, *npj Quantum Information* **6**, 8 (2020).
- [20] W. C. Smith, M. Villiers, A. Marquet, J. Palomo, M. Delbecq, T. Kontos, P. Campagne-Ibarcq, B. Douçot, and Z. Leghtas, *Physical Review X* **12**, 021002 (2022).
- [21] M. Hays, J. Kim, and W. D. Oliver, *PRX Quantum* **6**, 040321 (2025).
- [22] L. B. Nguyen, H. Kim, D. T. Le, T. Ersevimi, S. P. Chitta, T. Chistolini, C. Jünger, W. C. Smith, T. Stace, J. Koch, *et al.*, *arXiv preprint arXiv:2509.14656* (2025).
- [23] D. Feldstein-Bofill, L. U. Jakobsen, K. Shagalov, Z. Sun, C. Wied, S. Singh, A. Kringhøj, J. Hastrup, A. Gyenis, K. Flensberg, S. Krøjer, and M. Kjaergaard, *arXiv:2601.11303* (2026).
- [24] E. Roverc’h, A. Borgognoni, M. Villiers, K. Gerashchenko, W. C. Smith, C. Wilson, B. Douçot, A. Petrescu, P. Campagne-Ibarcq, and Z. Leghtas, *arXiv:2603.13114* (2026).
- [25] N. Didier, J. Bourassa, and A. Blais, *Phys. Rev. Lett.* **115**, 203601 (2015).
- [26] F. Pfeiffer, M. Werninghaus, C. Schweizer, N. Bruckmoser, L. Koch, N. J. Glaser, G. B. P. Huber, D. Bunch, F. X. Haslbeck, M. Knudsen, G. Krylov, K. Liegener, A. Marx, L. Richard, J. H. Romeiro, F. A. Roy, J. Schirk, C. Schneider, M. Singh, L. Södergren, I. Tsitsilin, F. Wallner, C. A. Riofrío, and S. Filipp, *Phys. Rev. X* **14**, 041007 (2024).
- [27] A. A. Chapple, O. Benhayoune-Khadraoui, S. Richer, and A. Blais, *Phys. Rev. Lett.* **135**, 256002 (2025).
- [28] C. Wang, F.-M. Liu, H. Chen, Y.-F. Du, C. Ying, J.-W. Wang, Y.-H. Huo, C.-Z. Peng, X. Zhu, M.-C. Chen, C.-Y. Lu, and J.-W. Pan, *Phys. Rev. Lett.* **135**, 060803 (2025).
- [29] G. Beaulieu, J.-Z. Chen, M. Scigliuzzo, O. Benhayoune-Khadraoui, A. A. Chapple, P. A. Spring, A. Blais, and P. Scarlino, *arXiv:2601.04975* (2026).
- [30] S. Hazra, W. Dai, T. Connolly, P. D. Kurilovich, Z. Wang, L. Frunzio, and M. H. Devoret, *Phys. Rev. Lett.* **134**, 100601 (2025).
- [31] K. Shagalov, D. Feldstein-Bofill, L. U. Jakobsen, Z. Sun, C. Wied, A. T. J. Paulsen, J. B. Severin, M. A. Marciniak, C. A. Potts, A. Kringhøj, J. Hastrup, K. Flensberg, S. Krøjer, and M. Kjaergaard, *arXiv preprint arxiv.2512.08470* (2025).
- [32] N. E. Frattini, U. Vool, S. Shankar, A. Narla, K. M. Sliwa, and M. H. Devoret, *Applied Physics Letters* **110**, 222603 (2017).
- [33] V. Sivak, N. Frattini, V. Joshi, A. Lingenfelter, S. Shankar, and M. Devoret, *Phys. Rev. Appl.* **11**, 054060 (2019).
- [34] B. Abdo, A. Kamal, and M. Devoret, *Phys. Rev. B* **87**, 014508 (2013).
- [35] K. S. Christensen, N. T. Zinner, and M. Kjaergaard, *Scheme for parity-controlled multi-qubit gates with su-*

- perconducting qubits (2023).
- [36] A. M. Bozkurt, J. Brookman, V. Fatemi, and A. R. Akhmerov, *SciPost Physics* **15**, 204 (2023).
- [37] L. Banszerus, W. Marshall, C. Andersson, T. Lindemann, M. Manfra, C. Marcus, and S. Vaitiekėnas, *Physical Review Letters* **133**, 186303 (2024).
- [38] L. Banszerus, C. Andersson, W. Marshall, T. Lindemann, M. Manfra, C. Marcus, and S. Vaitiekėnas, *Physical Review X* **15**, 011021 (2025).
- [39] A. Ciani, D. P. DiVincenzo, and B. M. Terhal, *Lecture Notes on Quantum Electrical Circuits* (TU Delft OPEN Books, 2025).
- [40] M. Rymarz and D. P. DiVincenzo, *Phys. Rev. X* **13**, 021017 (2023).
- [41] D. Feldstein-Bofill, Z. Sun, C. Wied, S. Singh, B. D. Isakov, S. Krøjer, J. Hastrup, A. Gyenis, and M. Kjaergaard, *Phys. Rev. Appl.* **24**, 044099 (2025).
- [42] C. Beenakker, *Physical review letters* **67**, 3836 (1991).
- [43] S. Rasmussen, K. Christensen, S. Pedersen, L. Kristensen, T. Bækkegaard, N. Loft, and N. Zinner, *PRX Quantum* **2**, 040204 (2021).